



Measuring water level in rivers and lakes from lightweight Unmanned Aerial Vehicles

Bandini, Filippo; Jakobsen, Jakob; Olesen, Daniel Haugård; Reyna-Gutiérrez, José Antonio; Bauer-Gottwein, Peter

Published in:
Journal of Hydrology

Link to article, DOI:
[10.1016/j.jhydrol.2017.02.038](https://doi.org/10.1016/j.jhydrol.2017.02.038)

Publication date:
2017

Document Version
Peer reviewed version

[Link back to DTU Orbit](#)

Citation (APA):
Bandini, F., Jakobsen, J., Olesen, D. H., Reyna-Gutiérrez, J. A., & Bauer-Gottwein, P. (2017). Measuring water level in rivers and lakes from lightweight Unmanned Aerial Vehicles. *Journal of Hydrology*, 548, 237-250. <https://doi.org/10.1016/j.jhydrol.2017.02.038>

General rights

Copyright and moral rights for the publications made accessible in the public portal are retained by the authors and/or other copyright owners and it is a condition of accessing publications that users recognise and abide by the legal requirements associated with these rights.

- Users may download and print one copy of any publication from the public portal for the purpose of private study or research.
- You may not further distribute the material or use it for any profit-making activity or commercial gain
- You may freely distribute the URL identifying the publication in the public portal

If you believe that this document breaches copyright please contact us providing details, and we will remove access to the work immediately and investigate your claim.

2

3

4 **Measuring water level in rivers and lakes from**

5 **lightweight Unmanned Aerial Vehicles**

6 Filippo Bandini^{*1}, Jakob Jakobsen², Daniel Olesen², Jose Antonio Reyna-Gutierrez¹, Peter Bauer-Gottwein¹

7 *Corresponding author: fban@env.dtu.dk

8 ¹*Department of Environmental Engineering, Technical University of Denmark, 2800, Lyngby, Denmark*

9 ²*National Space Institute, Technical University of Denmark, 2800, Lyngby, Denmark*

10

11 **Highlights**

- 12 •Water level of rivers and lakes can be measured by Unmanned Aerial Vehicles.
- 13 •Unmanned Aerial Vehicles ensure high accuracy and spatial resolution.
- 14 •The measuring system consists of a ranging sensor and a GNSS receiver.
- 15 •Among the ranging sensors, the radar has the highest accuracy and longest range.
- 16 •The camera-laser sensor is preferred for narrow field of view to water surface.

17

18 **Abstract**

19 The assessment of hydrologic dynamics in rivers, lakes, reservoirs and wetlands requires
20 measurements of water level, its temporal and spatial derivatives, and the extent and dynamics of
21 open water surfaces. Motivated by the declining number of ground-based measurement stations,
22 research efforts have been devoted to the retrieval of these hydraulic properties from spaceborne
23 platforms in the past few decades. However, due to coarse spatial and temporal resolutions,
24 spaceborne missions have several limitations when assessing the water level of terrestrial surface
25 water bodies and determining complex water dynamics. Unmanned Aerial Vehicles (UAVs) can
26 fill the gap between spaceborne and ground-based observations, and provide high spatial
27 resolution and dense temporal coverage data, in quick turn-around time, using flexible payload
28 design. This study focused on categorizing and testing sensors, which comply with the weight
29 constraint of small UAVs (around 1.5 kg), capable of measuring the range to water surface.
30 Subtracting the measured range from the vertical position retrieved by the onboard Global
31 Navigation Satellite System (GNSS) receiver, we can determine the water level (orthometric
32 height). Three different ranging payloads, which consisted of a radar, a sonar and an in-house
33 developed camera-based laser distance sensor (CLDS), have been evaluated in terms of
34 accuracy, precision, maximum ranging distance and beam divergence. After numerous flights,
35 the relative accuracy of the overall system was estimated. A ranging accuracy better than 0.5 %
36 of the range and a maximum ranging distance of 60 m were achieved with the radar. The CLDS
37 showed the lowest beam divergence, which is required to avoid contamination of the signal from
38 interfering surroundings for narrow fields of view. With the GNSS system delivering a relative
39 vertical accuracy better than 3-5 cm, water level can be retrieved with an overall accuracy better
40 than 5-7 cm.

41

42 Keywords: UAV; water level; radar; sonar; laser; GPS;

43 **1. Introduction**

44 Extreme hydro-climatic events such as droughts, floods and heavy precipitation have increased
45 the awareness that knowledge of spatial and temporal variation of open water surfaces is
46 important (Alsdorf et al., 2007). In order to achieve a better quantitative understanding of
47 hydrologic processes and to increase sharpness and reliability of hydrologic predictions,
48 observations of hydrological variables, such as surface water area, water level (h), its slope
49 ($\partial h/\partial x$) and its temporal change ($\partial h/\partial t$) are required. However, ground-based measurements of
50 terrestrial water bodies are limited to networks of measuring stations. In-situ stations provide
51 point observations that are often spaced too far apart to capture spatial patterns. Often, in-situ
52 observation technology fails during extreme events. Furthermore, globally, the availability of in-
53 situ hydrologic observation stations has been declining in the recent past (Lawford et al., 2013).
54 Hence, remote sensing datasets have become increasingly popular in hydrology. Remote sensing
55 techniques are presently unable to observe river discharge directly, however spatial and temporal
56 variation of water level has been routinely observed using spaceborne or airborne platforms.
57 Although most satellite altimetry missions were not designed primarily for monitoring
58 continental waters, water levels of continental water surfaces retrieved by Seasat,
59 TOPEX/Poseidon, Jason-1 and 2, GFO, ERS 1 and 2, ENVISAT have a measurement accuracy
60 that is well understood and generally on the order of a few tens of centimeters (Calmant et al.,
61 2008). This accuracy can be improved for larger lakes and rivers by averaging over large water
62 surfaces (Birkett, 1998; Birkett et al., 2002; Frappart et al., 2006). The satellite CryoSat-2 carries
63 a Synthetic Aperture Interferometric Radar Altimeter (SIRAL) which is a new generation radar
64 altimeter (Wingham et al., 2006) with a spatial resolution of around 300 m (Villadsen et al.,

65 2015). When operating in SARIn mode, a correction of the cross-track slope can be performed
66 and waveform analysis allows separation between water and surrounding topography
67 (Kleinherenbrink et al., 2014) resulting in an accuracy of the retrieved water level of just a few
68 decimeters (Kleinherenbrink et al., 2015). Spaceborne LIDARs such as the Geoscience Laser
69 Altimeter System (GLAS) have been shown to provide water level measurements with higher
70 accuracy than radar altimeters such as TOPEX/Poseidon (Zhang and Xie, 2010). Still, GLAS
71 has a ground footprint that is around 65 m (Schutz et al., 2005) and retrieves observations at
72 irregular temporal intervals. Therefore, the main limitations of conventional satellite radar and
73 laser altimetry are low spatial resolution, local coverage (for short repeat orbit missions) and low
74 temporal resolution (for long repeat missions such as CryoSat). In order to overcome these
75 limitations, the forthcoming Surface Water and Ocean Topography (SWOT) satellite mission
76 will build on the heritage of the imaging interferometric radars such as the Shuttle Radar
77 Topography Mission (SRTM) (Kiel et al., 2006; LeFavour and Alsdorf, 2005; Rodriguez et al.,
78 2006). However, spaceborne sensors will always face problems of: i) large ground footprints,
79 which result in relatively low spatial resolution; ii) fixed orbit configurations, which may be
80 inappropriate for high-resolution coverage of local water bodies; iii) coarse temporal resolution
81 and/or the non-regular revisit intervals. These limitations restrict their ability to measure the
82 temporal and spatial variation of the water level with the accuracy needed for determining the
83 hydraulics of complex rivers and flood waves.

84 Airborne LIDAR techniques have the advantages of better tracking of terrestrial water bodies,
85 improved spatial resolution, clear segmentation between land and water surfaces and a higher
86 accuracy (Schumann et al., 2008). However, airborne LIDAR surveys are expensive and their
87 success depends on surveying conditions (e.g. topography and geometry, vegetation cover, size

88 of the water body). For this reason, digital elevation models and digital surface models retrieved
89 by airborne LIDAR are not universally available and are normally not retrieved during periods of
90 hydrological interest such as flood events.

91 UAVs (Unmanned Aerial Vehicles) and in particular micro-UAVs (payload less than 1.5-2 kg),
92 represent the latest frontier in land and water monitoring because of low-altitude flight, low cost
93 and flexible payload design (Anderson and Gaston, 2013). In recent years, miniaturized
94 components (GNSS receivers, inertial measurement units, autopilots) have advanced (Watts et
95 al., 2012), and UAVs have been used also for a wide range of hydrological applications such as
96 fluvial monitoring; river bathymetry and photogrammetric DEM generation using very high
97 resolution (VHR) imagery (Lejot et al., 2007); water velocity measurements using large-scale
98 particle image velocimetry (LSPIV) (Detert and Weitbrecht, 2015; Tauro et al., 2016, 2015).

99 Moreover, UAVs have attracted great interest for monitoring of environmental disasters and
100 floods (Luo et al., 2015). UAVs are low-cost platforms that have unique capabilities to access
101 hostile or inaccessible environments that need to be urgently monitored. Moreover, they ensure
102 tracking of water surfaces better than satellite technology. However, for LIDAR and SAR
103 systems, the tradeoff between performance, cost and size/weight is still a challenge to be solved
104 before their application in UAV remote sensing (Colomina and Molina, 2014).

105 In this paper, we demonstrate the possibility to acquire measurements of water level by a ranging
106 system that includes a ranging sensor (radar, CLDS or sonar) and a GNSS receiver. The ranging
107 technology described in this paper provides water level measurements with higher accuracy than
108 spaceborne or airborne altimetry. Moreover, it ensures a spatial resolution ideal for measuring
109 the two dimensional spatial variability of small rivers and their interaction with floodplains (Lee
110 et al., 2011). Lastly, the newly developed CLDS can acquire ranges to water surfaces when only

111 narrow fields of view are available. The CLDS is specifically developed for applications in
112 vegetated environments or inside sinkholes in karst environments.

113 **2. Materials and Methods**

114 *2.1. General concept*

115 To acquire accurate water level (height above mean sea level) of open water surfaces, the UAV
116 must be equipped with: i) accurate lightweight sensors for measuring the range to water surface
117 ii) a high accuracy dual frequency GNSS receiver and antenna. Installation of an in-situ dual
118 frequency GNSS master station is needed for differential corrections. The general concept is
119 illustrated in Fig. 1.

120

121

122 **Fig. 1.**

123

124 The ellipsoidal height of the water surface is measured by subtracting the range measured by a
125 ranging sensor from the vertical position retrieved by the onboard GNSS receiver. Afterwards
126 the orthometric height can be retrieved from the ellipsoidal height if the geoid height is known
127 (Featherstone, 2001). For the purpose of this work, a hexacopter has been assembled from
128 TAROT-RC components and has been equipped with DJI Naza-M2 flight controller. The
129 hexacopter is able to fly at least 12 minutes carrying a payload of at most 2 kg. The choice of the
130 ranging sensors was constrained by: i) maximum weight of the payload, ii) a reasonable price
131 necessary for flexible operations, iii) sensor interfaces that allow time synchronization with the
132 GNSS receiver through a microprocessor. The selected ranging sensors included two off-the-

133 shelf sensors (a radar, a sonar) and the in-house developed CLDS. The total cost of the platform
134 is ca. 7000 euros. This cost includes the drone, the onboard GNSS system, the inertial
135 measurement unit (IMU), the three tested sensors and the microprocessor unit.

136 Fig. 2 shows the arrangement of the drone payload.

137

138 Fig. 2

139

140

141

142

143

144 *2.1.1. Radar ranger*

145 The radar is the ARS 30X model developed by Continental as anti-collision system for the
146 automotive industry (market price: 3200 EUR). It weighs around 350 g and consists of a 77 GHz
147 radar sensor with a mechanical scanning antenna. It measures the range to targets using FMCW
148 (Frequency Modulated Continuous Wave) with a sampling frequency of 15 measurements per
149 second. It provides up to 32 targets in near range and up to 64 targets in far range with a
150 resolution of 0.10 m. Each individual target angle is provided with a resolution of 0.1°.

151 *2.1.2. Sonar ranger*

152 The sonar is the MB7386 model from MaxBotix (market price: 150 EUR). It weighs around 50g
153 and consists of a 42 kHz ultrasonic sensor (6 Hz reading rate) with internal temperature

154 compensation, noise tolerance and clutter rejection. Its maximum ranging capability is up to 10
155 m.

156 2.1.3. *Camera-based laser distance sensor (CLDS)*

157 This ranging sensor is a laser camera-based solution recently developed at Technical University
158 of Denmark (Reyna Gutierrez, 2013). It weighs around 350 g. It was inspired by the measuring
159 procedure proposed by Danko (2004). The range distance to the target is estimated by measuring
160 the angle at which laser light enters the camera. The original methodology is expanded in this
161 work to include corrections for tilting and rotation angles of the aircraft. An efficient automatic
162 algorithm for identifying the laser dots on the water surface was developed. Our prototype
163 consists of two laser pointers (100 mW laser diodes) and a complementary metal–oxide–
164 semiconductor (CMOS) camera. The camera resolution is 20.2 megapixels. The camera is
165 triggered by the on-board single board computer (SBC) with an image rate of 1 frame every 2.5
166 seconds. The total manufacturing cost of this CLDS system is around 800 EUR. The current
167 design of the distance-meter includes a digital camera mounted at the center between the two
168 laser pointers. Fig. 3 shows the geometrical configuration of the camera. Range to water surface
169 is measured by illuminating the water surface with the laser pointers and taking a picture of the
170 illuminated water surface. When light emitted by laser pointers hits the water surface, bright dots
171 are formed at the interface between water and air. Due to scattering processes (in particular
172 Rayleigh and Mie scattering), some portion of the radiation is reflected in the direction of the
173 camera and an estimation of the range to water surface is possible.

174

175 Fig. 3.

176 The angle α is a design parameter. The CLDS was built with $\alpha = 90^\circ$ to simplify the measuring
177 concept and the derivation of the formulas. The CLDS shown in Fig. 3 is exactly symmetrical.
178 Indeed, only one laser would be sufficient to acquire the range to the surface; nevertheless, two
179 laser pointers improve error assessment and system accuracy.
180 The value of the measured range H_m can be computed by measuring the angle θ' at which light
181 enters the camera, i.e. from equation (1).

$$H_m = \frac{A}{\tan \theta'} \quad (1)$$

182
183 Alternatively, the measured range H_m can be obtained through equation (2)

$$H_m = \frac{A \cdot f}{ImD} \quad (2)$$

184 Where ImD (Image distance) is the distance between the center of the image and the recorded
185 light source. A calibration procedure is needed to convert from the number of pixels from the
186 center of the image (PFC) to ImD as shown in equation (3)

$$ImD = PFC \cdot d_{pp1} + d_0 \quad (3)$$

187 Where d_{pp1} and d_0 are the coefficients of the first-order polynomial producing the best least-
188 squares fit to the data. Equations (2) and (3) can be applied only when the focal length (f) of the
189 camera is exactly and the focus is constantly set to infinity. Otherwise, the calibration procedure
190 needs to estimate the angle θ' directly from the number of pixels (PFC) as shown in equation (4).

$$\theta' = PFC \cdot r_{pp1} + r_0 \quad (4)$$

191 Where r_{pp1} and r_0 are the coefficients of the first-order polynomial producing the best least-
192 squares fit to the data. The calibration procedure, which has to be performed to estimate the r_{pp1}
193 and r_0 coefficients, is presented in the appendix. The calibration procedure allows estimation of
194 the angle θ' by measuring PFC, without having to consider the linear or nonlinear intrinsic
195 camera parameters, such as focal length and lens distortion.

196 Onboard the UAV, tilting and rotation cause a displacement of the light sources from their
197 equilibrium position. The changes in the geometrical relationships generate an error in the
198 estimation of the true range distance (hereafter defined as H_t) between the sensor of the camera
199 and the water surface. Tilting is the angle between the plane on which the camera and laser are
200 located, i.e. the axis of the CLDS, and the horizontal plane (angle β as shown in Fig. 4). Rotation
201 occurs between the vertical line and the optical axis of the camera (angle δ as shown in Fig. 5).

Fig. 4

Fig. 5

202 If tilting pushes the light source below the axis of the distance meter, formula (5) can be used to
203 obtain the true range (H_t) between the camera and the water surface:

$$H_t = [(H_m + A \cdot \tan \beta) \cos \beta] \cdot \cos \delta \quad (5)$$

204 Conversely, if the tilting pushes the light source above the axis of the CLDS, formula (6) can be
 205 used:

$$H_t = [(H_m - A \cdot \tan \beta) \cos \beta] \cdot \cos \delta \quad (6)$$

206 If pitch and roll angles are retrieved on board the UAV, the measured range can be corrected
 207 according to equation (5) and (6) (Reyna Gutierrez, 2013). If the angles are not retrieved on
 208 board, the resulting error on the range can be estimated as shown in Fig. 6. Numerous tests have
 209 been conducted in order to determine the best configuration of the CLDS in terms of: i) arm
 210 length A, ii) wavelengths of the two laser pointers, iii) optimal camera configuration parameters
 211 such as optical zoom and resolution.

212 The arm length choice affects the measuring range function, as shown in Fig. 7.

Fig. 6

Fig. 7

213 Fig. 7 shows that the resolution of the measurements depends on the derivative of the range
 214 function. Hence, a longer arm will result in higher resolution, especially for longer ranges.
 215 Indeed, in Fig. 7, the smoothest curve is for an arm length of 0.6 m. However, the payload size of
 216 small UAVs is limited and thus a 30 cm arm was chosen for our tests. The wavelengths of the
 217 two laser pointers were chosen as 450 nm and 531 nm, because reflectivity of water is relatively

218 high at these wavelengths as a consequence of the optical proprieties of water as described in
219 Hale and Query (1973).
220 When the laser light hits the water surface, a bright dot is formed at the point of contact.
221 However, additional bright spots might be visible due to reflection from the riverbed and due to
222 additional scattering processes caused by water waves. To identify the two dots formed by laser
223 reflection, an automatic identification algorithm was developed consisting of the following
224 computational steps: i) the RGB image is converted to Hue, Saturation and Value (HSV) image.
225 Quasi-circular shapes in the image are found through circular Hough transform (Yuen et al.,
226 1990). In case there are multiple circles in the image, the two circles (one generated by the left
227 laser and one by the right laser) with the highest mean Value (V) are considered to be the contact
228 spots. Thereafter, ii) the brightest pixel (pixel with the highest Value) is identified inside each of
229 the two circles (laser dots). The brightest pixel typically lies in the center of the laser dot in case
230 of normal light incidence. Lastly, iii) the distance (PFC) between the center of the image and the
231 two identified brightest pixels is computed. Post-processing of the images is performed after the
232 flight and takes around 30 seconds per image.

233 *2.1.4. GNSS system*

234 The differential GNSS system consists of two NovAtel receivers: one used as master station
235 (flexpack6) and one as rover (OEM628 board). A NovAtel GPS-703-GGG pinwheel triple
236 frequency and GLONASS antenna is used as base station and an antcom (3G0XX16A4-XT-1-4-
237 Cert) dual frequency GPS and GLONASS flight antenna is used as rover station on the UAV.
238 Raw pseudoranges and carrier phase measurements are stored at 5 Hz. The position solution is
239 post-processed using Leica Geomatic Office v 8.1 in kinematic mode. In post-processed mode, a
240 Kalman filter can be applied both in forward and backward direction for best position

241 performance. The length of the GPS baseline affects the vertical and horizontal accuracy of the
242 drone position. Position error is expected to increase by 1-3 ppm (1-3 mm additional error per
243 km of baseline).

244

245 *2.1.5. Payload controller*

246 Data acquired by the different sensors are saved on the SBC (BeagleBone Black) and a time
247 synchronization of the different sensors can be performed. Synchronization between the position
248 retrieved by the GNSS system and the range retrieved by the sensors is essential for accurate
249 water level observations, as described in Appendix B.

250

251 *2.2. Testing of the sensors*

252 To test the accuracy of the system, both static (ground-based) and dynamic (airborne) tests were
253 performed. First, several tests were conducted from bridges of different heights over free-flowing
254 rivers in order to test accuracy, precision and maximum ranging capability. Beam divergence
255 was tested by acquiring measurements inside a water well of small diameter. After the ground-
256 based tests, numerous flight tests were conducted over a lake. Because the water level in the lake
257 can be assumed to be uniform in space, these flights allowed determination of the accuracy of the
258 full system, which consists of the GNSS receiver and the ranging sensors. Appendix B reports
259 the experimental settings of both static and airborne tests.

260

261 2.2.1. *Ground-based evaluation*

262 Accuracy of the ranging sensors was estimated using as reference a water level dip meter, which
263 has an accuracy better than 0.3% of the range. When tested in static mode, sensors acquired
264 measurements for 30 seconds. Subsequently the average range (\bar{x}) was computed as the weighted
265 arithmetic mean as shown in equation (7) after outlier removal ($\geq 5\sigma$).

$$\bar{x} = \frac{\sum_{i=1}^N f_i x_i}{\sum_{i=1}^N f_i} \quad (7)$$

266

267 In equation (7) x_i is an observation and f_i the frequency of that value. N is the total number of
268 measurements which depends on the reading range of the individual sensor.

269 Precision is estimated as standard deviation (σ) of the measuring stack, and is computed using
270 equation (8):

$$\sigma = \sqrt{\frac{\sum_{i=1}^N f_i \cdot (x_i - \bar{x})^2}{\sum_{i=1}^N f_i - 1}} \quad (8)$$

271

272 Maximum ranging capability is the maximum range from which the sensor can retrieve a
273 measurement with a reasonable accuracy (i.e. 5% of the range).

274 Beam divergence is defined as the measure (in angular units) of the increment in beam
275 diameter with distance from the optical aperture or antenna from which the sonic or
276 electromagnetic beam emerges. A larger beam divergence leads to a larger ground footprint of
277 the signal, which results in contamination of the signal if the surface is inhomogeneous. For the
278 CLDS this parameter is negligible, since its ground footprint directly depends on the arm length
279 A and the laser beam divergence is very low. Moreover, the CLDS provides images of each
280 individual acquisition and the user can perform a-posteriori supervision to control if the

281 measured target is indeed the water surface. For the radar and the sonar, beam divergence is a
282 critical parameter to ensure that water is measured without interference from the surroundings.
283 This parameter has to be considered in order to monitor water bodies (e.g. large sinkholes, rivers
284 surrounded by dense vegetation), which only expose a narrow stretch of water to aerial view.
285 Indeed, because of loss of GNSS signal, flights under vegetation canopy or inside small cavities
286 (e.g. karst sinkholes) cannot be performed without losing position accuracy. Beam divergence
287 was estimated by acquiring measurements over water wells of small diameter, while water was
288 gradually being pumped out, as described in Appendix B.

289 *2.2.2. Airborne evaluation*

290 Numerous flights were conducted above a 0.02 km² lake located near Holte, Denmark
291 (55.821720°N, 12.509067°E). Water level in the lake is practically uniform. Whilst the sonar
292 and the CLDS identify only one target in the field of view, the radar can identify multiple targets
293 and reports the target angle for each of those. This requires an accurate identification of the
294 target, which is representative of the water surface. Indeed, sometimes multiple targets are
295 retrieved at nadir angle, for instance when vegetation is overhanging the water body. In that case,
296 postprocessing requires switching between different targets to obtain a result that is continuous
297 in time. Moreover, a low-pass digital filter was applied on the 15Hz raw radar data. A weighted
298 moving average (WMA) with a temporal window of 0.33 s (five observations) was applied to
299 smoothen the signal as shown in equation (9).

$$WMA_t = w_1 A_{t-2} + w_2 A_{t-1} + w_3 A_t + w_4 A_{t+1} + w_5 A_{t+2} \quad (9)$$

300

301 Weights ($w_1, w_2 \dots w_5$) are normally set to a high value for the measurement taken at the actual
302 time (A_t) and to lower values for the previous and subsequent measurements.

303 .The overall accuracy of the system consisting of the GNSS receiver and the ranging sensor
304 (σ_{tot}) is assumed to be that of two independent normally distributed variables: the ranging sensor
305 accuracy and the GNSS accuracy (10).

$$\sigma_{tot} = \sqrt{\sigma_s^2 + \sigma_{RTK}^2} \quad (10)$$

306

307 where σ_s is the accuracy of the ranging sensor and σ_{RTK} is the accuracy of the GNSS receiver.

308 **3. Results**

309 The first section of the results describes the technical performance of the ranging sensors when
310 tested from a static position on the ground. Results are based on numerous tests conducted from
311 bridges of different heights to compare the technical performance of the different sensors. The
312 second section describes the results of the flight tests that are intended to evaluate the accuracy
313 of the integrated system, i.e. GNSS receiver and sensors operating on board the UAV.

314 *3.1. Ground-based performance results*

315 Sensors demonstrated different performance in terms of accuracy and standard deviation of the
316 measuring stack when tested from bridges of different heights. Appendix B lists the experimental
317 settings for the static tests. Fig. 8 shows that the sonar usually tends to overestimate the range to
318 water surface, which is probably caused by a slight penetration of the ultrasonic wave (42 kHz)
319 below the water surface. Conversely, the radar usually tends to underestimate the range. The

320 authors guess that this is due to the post-processing of the raw data by the proprietary radar
321 firmware.

322

323

324 Fig. 8

325

326

327 Table 1 summarizes the sensors' technical performance in terms of accuracy, standard deviation
328 of the measurement stack, maximum ranging distance and beam divergence.

329

330 Table 1

331

332 Table 1 confirms that the sonar is the best sensor in terms of accuracy and standard deviation of
333 the measurement stack. The CLDS has the lowest beam divergence. However, the radar is the
334 sensor that combines the longest ranging capability, with accuracy and standard deviation that
335 are only slightly worse than for the sonar. In Fig.9, two regression lines confirm the systematic
336 error of radar and sonar. Plotted as function of the range, the regression line of the radar absolute
337 error has a slope of -0.0090 , while the slope of the sonar is 0.0083 . After removal of this
338 systematic error, the radar shows an accuracy of 0.5% of the range, whilst the accuracy of the
339 sonar is around 0.3% .

340

341

342 Fig.9

343

344

345 Finally, the accuracy of the retrieved vertical position has to be assessed. The accuracy of the
346 GNSS height depends mainly on: i) the integer ambiguity solution that has to be fixed to obtain
347 reliable observations, ii) the satellite geometry that affects the dilution of precision (DOP), iii)
348 multipath interference, especially because of signal reflection from the water surface.

349

350 *3.2. Airborne performance results*

351 In this section, we report the observations of two flights and we show a table summarizing the
352 entire dataset of flights over the lake. The range measured by each of the sensors and the altitude
353 retrieved by the GNSS are shown in Fig.10. The figure contains the entire dataset of observations
354 retrieved by the radar and sonar. Only not-a-number (NaN) values are removed. The sonar
355 outputs NaN when the range exceeds the maximum range capability (10 m). For the CLDS, we
356 only reported the measurements retrieved from images in which the laser dots are clearly
357 identifiable on the water surface.

358

359 Fig.10

360

361 Fig.10 shows an extremely high correlation (Pearson coefficient of 0.9991), between the GNSS
362 and the radar measurements, which indicates the consistency of our ranging technology. The
363 laser dots are generally distinguishable on the water surface only when the range to water surface
364 is less than 12-13 m . Similarly, the sonar provided accurate measurements only when the UAV

365 was hovering at low altitudes (less than 10 m from the water surface). Indeed, the radar and
366 sonar curves only overlap during these flight maneuvers.

367 In Fig. 11 we display the water level measured by the different sensors. Outliers ($>2\sigma$) were
368 removed.

369

370 Fig. 11

371

372 Mode value, mean and standard deviation of water level retrieved by each of the sensors are
373 reported in Table 2 under the column with flight date “04/04”. The dispersion in water level
374 measurements retrieved by the system consisting of the radar and the GNSS receiver may be due
375 to multipath errors on the GNSS receiver. The cut-off angle for the elevation of the satellites,
376 which defines the angle below which GPS satellites are excluded, turned out to be a sensitive
377 parameter. The selected values for each flight are reported in Appendix B.

378 The water level values retrieved by the sonar had low accuracy, especially during high-speed
379 maneuvers. Since the range to water surface was greater than the maximum range capability of
380 the sonar for a significant portion of flight duration, the sonar retrieved many NaN values and
381 noisy observations. However, the mode value retrieved by the sonar is 24.14 m, which is close to
382 the mean value retrieved by the radar.

383 The CLDS exhibits only few observations due to limited range capability and low frame rate.

384 Moreover, natural light conditions complicate the recognition of the laser dots on the water
385 surface.

386 In order to estimate the absolute accuracy of the sensors, results were compared to in-situ
387 measurements of water level. For the in-situ measurement, an additional accurate RTK (Real

388 Time Kinematic) GNSS rover station was used, which was connected to a Danish GPS network.
389 The position was averaged over a period of one minute which resulted in 24.10 m above the
390 DVR90 geoid model (with an estimated accuracy of the GNSS rover station of around 5-6 cm).
391 For this flight, the accuracy of the radar is thus better than 5 cm, the mode value of the sonar is
392 around 4 cm from the ground truth, while the mean value retrieved by the CLDS is within two
393 decimeters.

394 The second flight reported in Fig. 12 evaluated performance for higher drone altitude (up to 60
395 m) above the water surface.

396

397 Fig. 12

398 As shown in Fig. 12, the radar and the GNSS show very high correlation for the entire flight.
399 The flight confirmed the limited ranging capability of the sonar (specified as 10 m, but already
400 very noisy beyond 9 m). The CLDS retrieved ranges up to 13 m, however standard deviations
401 increased significantly with range. In Fig. 13 we compare the water level retrieved by the three
402 different sensors for this flight.

403

404 Fig. 13

405

406 Statistics of the flight are shown in Table 2 under the column “27/05”. In-situ water level was
407 24.01 m. Fig. 13 shows that the sonar measurements were unsuccessful. The CLDS, despite very
408 high standard deviations, shows a mean value that is very close to the ground truth. The radar
409 shows higher dispersion for long ranges. Moreover, systematic error is still observable, in fact

410 when the drone is at higher altitude, the retrieved water level increases by a few cm. System
411 performance was confirmed in a number of other flights, as shown in Table 2 . Experimental
412 settings, such as flight speed, illumination conditions, sensor settings for each flight, are
413 explained in appendix B.

414

415

416 Table 2

417

418 Table 2 clearly indicates that the radar is the most reliable sensor, with the lowest standard
419 deviation and good agreement with in-situ measurements. However, during some of the flights,
420 the measured water level exhibits significant standard deviation also for the radar. This
421 dispersion of the water level observations is caused not only by ranging errors but also by the
422 GNSS. Indeed, during some flights, the geometrical configuration of GNSS satellites may have
423 been suboptimal for accurate positioning. In addition to this, multipath of the GNSS signal may
424 occur and degrade the accuracy of water level observations to ca. 7 cm.

425 The sonar provides very noisy measurements and exhibits a skewed distribution with a fat tail
426 around 10 m, which is the maximum range of the sensor. While the mean value of water level
427 does not provide an accurate estimate, the mode values measured by the sonar are very similar to
428 the corresponding values measured by the radar.

429 For the CLDS, the mode value is not relevant because the number of observations is low. The
430 CLDS standard deviation is quite large and in order to obtain accurate results the drone has to
431 hover for several seconds.

432 **4. Discussion**

433 The ranging technology showed great potential in terms of accuracy, maximum range and beam
434 divergence. In particular, the radar demonstrated the best performance in terms of accuracy and
435 maximum range. The ranging sensor has to be integrated with carrier phase differential GNSS to
436 retrieve water level. The accuracy of the integrated system consisting of GNSS receiver and
437 radar is estimated to be better than 5-7 cm. This accuracy can be compared with the accuracy
438 achievable with: i) airborne LIDARs, ii) spaceborne laser altimetry, iii) spaceborne radar
439 altimetry and iv) ground-based stations as shown in Table 3.

440

441

442

443 Table 3

444

445

446 Few studies report the accuracy of LIDAR system in measuring water surface, but it has been
447 estimated to vary from few cm up to two tens of cm (Hopkinson et al., 2011). For airborne
448 LIDAR systems, the inaccuracy of the onboard positioning systems has to be included. Similarly
449 spaceborne laser altimetry from ICESat, which is the satellite altimeter with the smallest
450 footprint (50–90 m) and the highest along-track resolution (40 Hz, 170 m), provides water
451 surface elevation measurements for rivers with an accuracy at decimeter level. However the
452 accuracy degrades in case of cloud cover (Phan et al., 2012). Additionally, simultaneous return
453 from land and water are inevitable for small rivers and the identification of water surfaces
454 remains problematic. The accuracy of radar altimetry sensors such as the systems on board

455 Jason-2 (Asadzadeh Jarihani et al., 2013), Envisat (Frappart et al., 2006) and Cryosat-2 (Song et
456 al., 2015) is in the order of some tens of dm. Moreover, satellite radar altimetry generally has a
457 spatial resolution lower than satellite laser altimetry and requires that rivers are hundreds of
458 meters wide to avoid signal contamination by interfering land and vegetation (Maillard et al.,
459 2015). With UAV-borne monitoring, water surface and interfering surroundings can be clearly
460 separated due to the smaller ground footprint, and the possibility to retrieve individual radar
461 target angles. However, for very narrow fields of view, the CLDS is the only sensor that can
462 provide reliable water level measurements. Image analysis as part of the post-processing
463 workflow ensures that measurement are accepted only if the monitored target is the water
464 surface. This is the case for rivers surrounded by dense riparian vegetation or for small targets
465 such as karst sinkholes, e.g. on the Yucatán Peninsula (Gondwe et al., 2010). Our CLDS solution
466 overcomes the limitations of traditional red wavelength time-of-flight (TOF) laser distance
467 meters, which are not suitable for ranging to water surfaces, because the reflectivity of water is
468 very low for red visible wavelengths.

469 Only ground-based hydrometric stations ensure an accuracy higher than the one achieved with
470 UAV-based monitoring, but coverage and reliability of in-situ monitoring networks have been
471 degrading in many regions of the world. Moreover, despite providing high accuracy and
472 temporal resolution, in-situ stations acquire only local measurements and tend to fail during
473 extreme events. Therefore, UAV-based water level monitoring is beneficial for the monitoring of
474 a wide range of hydrological systems, including small-scale rivers, ephemeral lakes, sinkholes,
475 meltwater lakes, etc... UAV-based water level observations can resolve the spatial
476 multidimensional variability of rivers. Indeed, UAVs can monitor water level along and across
477 the river course, in order to obtain water slope and assess interaction between rivers and adjacent

478 floodplains. Improved sharpness and reliability of estimates of surface water-groundwater
479 interaction using UAV-based monitoring of river water levels have already been reported
480 (Bandini et al., 2016). Furthermore, UAVs can sense water level in unconventional remote
481 sensing targets such as sinkholes or cenotes. This could potentially improve mapping of phreatic
482 surfaces, for instance for the Yucatan peninsula (Bauer-Gottwein et al., 2011). Additionally,
483 UAVs can potentially be used during extreme events when in-situ monitoring stations often fail
484 and satellite observations do not ensure the required spatial and temporal resolution. Thus, UAVs
485 have the potential to improve flood risk assessment. However, the $\pm 7\text{cm}$ accuracy of our
486 technology may still be insufficient for rivers flowing through low-lying terrain. Nonetheless, the
487 accuracy is better than other spaceborne and airborne technologies and UAVs have a great
488 potential in improving flood mapping because they allow optimal timing of the observations and
489 high spatial resolution. UAV-based observations of water level in the flooded areas allow
490 determination of stage-damage curves (Cammerer et al., 2013) which are essential for the design
491 of insurance policies.

492 **5. Conclusions**

493 UAV-based remote sensing of river and lake water level (orthometric height) has the potential to
494 fill the gap between in-situ measurements and spaceborne remote sensing. It ensures: i) high
495 accuracy, ii) optimal spatial resolution, iii) flexible timing of the sampling, and iv) precise
496 tracking of lakes and rivers. Different water surface ranging sensors were tested: a radar, a sonar,
497 and a CLDS.

498 Static (on ground) and dynamic (airborne) tests demonstrated the following results:

- 499 • The radar showed the best accuracy and longest maximum range. Despite having a
500 resolution of only 10 cm, averaging the 15 Hz primary data, an accuracy of 0.5% of the
501 range can be achieved after correction of a negative bias of 0.9% of the range.
- 502 • The sonar provided unreliable results for high ranges or high speeds. Our results show
503 that the sonar generally overestimates the range to water surface. However, when the
504 UAV flies at a stable and low height, the accuracy is down to a few centimeters.
- 505 • The CLDS is less accurate than the radar. However, it has the lowest beam divergence
506 and is useful when only a narrow field of view to the water surface is available for
507 sensing.

508 Water level can be measured on board UAVs by subtracting the range to water surface from
509 the vertical position retrieved by the GNSS receiver. Dynamic (airborne) tests have been
510 performed on the positioning technology and the GNSS receiver had a vertical accuracy
511 around 4-6 cm (2σ) and had an expected horizontal accuracy around 2 cm (2σ). However,
512 multipath of the GNSS signal causes problems above water and the choice of the cut-off
513 satellite elevation angle has a considerable influence on the position accuracy.

514 The integrated system GNSS receiver and radar is able to measure water level with an overall
515 accuracy better than 5-7 cm when the UAV flies at a speed of few km/h.

516 Future research should include different types of sonar sensors, trading off signal penetration
517 below the water surface (more penetration at lower frequencies) and interference of the propeller
518 noise (more interference at higher frequencies). Moreover, research efforts are ongoing to
519 develop new radars with higher measurement resolution, exploiting other region of the
520 microwave spectrum commonly used in radar altimetry such as Ku and Ka bands.

521

522

523

524 The master thesis from Reyna Gutierrez, J. A. (2013) ‘‘Monitoring and modeling of regional
525 groundwater flow on the Yucatán Peninsula’’ can be obtained from the authors upon request.

526 **Acknowledgements**

527 The Innovation Fund Denmark is acknowledged for providing funding for this study via the
528 project Smart UAV [125-2013-5].

529 **References**

- 530 Alsdorf, D.E., Rodriguez, E., Lettenmaier, D.P., 2007. Measuring surface water from space. *Rev.*
531 *Geophys.* 45, 1–24. doi:10.1029/2006RG000197.1
- 532 Anderson, K., Gaston, K.J., 2013. Lightweight unmanned aerial vehicles will revolutionize
533 spatial ecology. *Front. Ecol. Environ.* 11, 138–146. doi:10.1890/120150
- 534 Asadzadeh Jarihani, A., Callow, J.N., Johansen, K., Gouweleeuw, B., 2013. Evaluation of
535 multiple satellite altimetry data for studying inland water bodies and river floods. *J. Hydrol.*
536 505, 78–90. doi:10.1016/j.jhydrol.2013.09.010
- 537 Bandini, F., Butts, M., Vammen Torsten, J., Bauer-Gottwein, P., 2016. Water level observations
538 from Unmanned Aerial Vehicles (UAVs) for improving probabilistic estimations of
539 interaction between rivers and groundwater. *Geophys. Res. Abstr.* 18, EGU2016-3144.
- 540 Bauer-Gottwein, P., Gondwe, B.R.N., Charvet, G., Marin, L.E., Rebolledo-Vieyra, M., Merediz-
541 Alonso, G., 2011. Review: The Yucatan Peninsula karst aquifer, Mexico. *Hydrogeol. J.* 19,
542 507–524. doi:10.1007/s10040-010-0699-5
- 543 Birkett, C.M., 1998. Contribution of the TOPEX NASA Radar Altimeter to the global
544 monitoring of large rivers and wetlands. *Water Resour. Res.* 34, 1223.
545 doi:10.1029/98WR00124
- 546 Birkett, C.M., Mertes, L. a K., Dunne, T., Costa, M.H., Jasinski, M.J., 2002. Surface water
547 dynamics in the Amazon Basin: Application of satellite radar altimetry. *J. Geophys. Res.*
548 *Atmos.* 107, LBA-26. doi:10.1029/2001JD000609
- 549 Calmant, S., Seyler, F., Cretaux, J.F., 2008. Monitoring continental surface waters by satellite
550 altimetry. *Surv. Geophys.* 29, 247–269. doi:10.1007/s10712-008-9051-1
- 551 Cammerer, H., Thielen, A.H., Lammel, J., 2013. Adaptability and transferability of flood loss

- 552 functions in residential areas. *Nat. Hazards Earth Syst. Sci.* 13, 3063–3081.
553 doi:10.5194/nhess-13-3063-2013
- 554 Colomina, I., Molina, P., 2014. Unmanned aerial systems for photogrammetry and remote
555 sensing: A review. *ISPRS J. Photogramm. Remote Sens.* 92, 79–97.
556 doi:10.1016/j.isprsjprs.2014.02.013
- 557 Danko, T., 2004. Webcam Based DIY Laser Rangefinder [WWW Document]. URL
558 https://sites.google.com/site/todddanko/home/webcam_laser_ranger (accessed 11.9.15).
- 559 Detert, M., Weitbrecht, V., 2015. A low-cost airborne velocimetry system: proof of concept. *J.*
560 *Hydraul. Res.* 53, 532–539. doi:10.1080/00221686.2015.1054322
- 561 Featherstone, W.E., 2001. Absolute and relative testing of gravimetric geoid models using
562 Global Positioning System and orthometric height data. *Comput. Geosci.* 27, 807–814.
563 doi:10.1016/S0098-3004(00)00169-2
- 564 Frappart, F., Calmant, S., Cauhopé, M., Seyler, F., Cazenave, A., 2006. Preliminary results of
565 ENVISAT RA-2-derived water levels validation over the Amazon basin. *Remote Sens.*
566 *Environ.* 100, 252–264. doi:10.1016/j.rse.2005.10.027
- 567 Gondwe, B.R.N., Lerer, S., Stisen, S., Marín, L., Rebolledo-Vieyra, M., Merediz-Alonso, G.,
568 Bauer-Gottwein, P., 2010. Hydrogeology of the south-eastern Yucatan Peninsula: New
569 insights from water level measurements, geochemistry, geophysics and remote sensing. *J.*
570 *Hydrol.* 389, 1–17. doi:10.1016/j.jhydrol.2010.04.044
- 571 Hale, G.M., Querry, M.R., 1973. Optical Constants of Water in the 200-nm to 200-microm
572 Wavelength Region. *Appl. Opt.* 12, 555–563. doi:10.1364/AO.12.000555
- 573 Hopkinson, C., Crasto, N., Marsh, P., Forbes, D., Lesack, L., 2011. Investigating the spatial
574 distribution of water levels in the Mackenzie Delta using airborne LiDAR. *Hydrol. Process.*
575 25, 2995–3011. doi:10.1002/hyp.8167
- 576 Kiel, B., Alsdorf, D., LeFavour, G., 2006. Capability of SRTM C- and X-band DEM Data to
577 Measure Water Elevations in Ohio and the Amazon. *Photogramm. Eng. Remote Sens.* 72,
578 313–320. doi:10.14358/PERS.72.3.313
- 579 Kleinherenbrink, M., Ditmar, P.G., Lindenbergh, R.C., 2014. Retracking Cryosat data in the
580 SARIn mode and robust lake level extraction. *Remote Sens. Environ.* 152, 38–50.
581 doi:10.1016/j.rse.2014.05.014
- 582 Kleinherenbrink, M., Lindenbergh, R.C., Ditmar, P.G., 2015. Monitoring of lake level changes
583 on the Tibetan Plateau and Tian Shan by retracking Cryosat SARIn waveforms. *J. Hydrol.*
584 521, 119–131. doi:http://dx.doi.org/10.1016/j.jhydrol.2014.11.063
- 585 Lawford, R., Strauch, A., Toll, D., Fekete, B., Cripe, D., 2013. Earth observations for global
586 water security. *Curr. Opin. Environ. Sustain.* 5, 633–643. doi:10.1016/j.cosust.2013.11.009
- 587 Lee, H., Beighley, R.E., Alsdorf, D., Jung, H.C., Shum, C.K., Duan, J., Guo, J., Yamazaki, D.,
588 Andreadis, K., 2011. Characterization of terrestrial water dynamics in the Congo Basin
589 using GRACE and satellite radar altimetry. *Remote Sens. Environ.* 115, 3530–3538.
590 doi:10.1016/j.rse.2011.08.015

- 591 LeFavour, G., Alsdorf, D., 2005. Water slope and discharge in the Amazon River estimated
592 using the shuttle radar topography mission digital elevation model. *Geophys. Res. Lett.* 32,
593 L17404. doi:10.1029/2005GL023836
- 594 Lejot, J., Delacourt, C., Piégay, H., Fournier, T., Trémélo, M.-L., Allemand, P., 2007. Very high
595 spatial resolution imagery for channel bathymetry and topography from an unmanned
596 mapping controlled platform. *Earth Surf. Process. Landforms* 32, 1705–1725.
597 doi:10.1002/esp.1595
- 598 Luo, C., Nightingale, J., Asemota, E., Grecos, C., 2015. A UAV-Cloud System for Disaster
599 Sensing Applications, in: 2015 IEEE 81st Vehicular Technology Conference (VTC Spring).
600 IEEE, pp. 1–5. doi:10.1109/VTCSpring.2015.7145656
- 601 Maillard, P., Bercher, N., Calmant, S., 2015. New processing approaches on the retrieval of
602 water levels in Envisat and SARAL radar altimetry over rivers: A case study of the São
603 Francisco River, Brazil. *Remote Sens. Environ.* 156, 226–241.
604 doi:10.1016/j.rse.2014.09.027
- 605 Phan, V.H., Lindenbergh, R., Menenti, M., 2012. ICESat derived elevation changes of Tibetan
606 lakes between 2003 and 2009. *Int. J. Appl. Earth Obs. Geoinf.* 17, 12–22.
607 doi:10.1016/j.jag.2011.09.015
- 608 Reyna Gutierrez, J.A., 2013. Monitoring and modeling of regional groundwater flow on the
609 Yucatán Peninsula. Unpubl. master's thesis, Tech. Univ. Denmark.
- 610 Rodriguez, E., Morris, C., Belz, J., 2006. An assessment of the SRTM topographic products.
611 *Photogramm. Eng. Remote Sensing* 72, 249–260. doi:0099-1112/06/7203-0249/\$3.00/0
- 612 Schumann, G., Matgen, P., Cutler, M.E.J., Black, a., Hoffmann, L., Pfister, L., 2008.
613 Comparison of remotely sensed water stages from LiDAR, topographic contours and
614 SRTM. *ISPRS J. Photogramm. Remote Sens.* 63, 283–296.
615 doi:10.1016/j.isprsjprs.2007.09.004
- 616 Schutz, B.E., Zwally, H.J., Shuman, C. a., Hancock, D., DiMarzio, J.P., 2005. Overview of the
617 ICESat mission. *Geophys. Res. Lett.* 32, 1–4. doi:10.1029/2005GL024009
- 618 Song, C., Ye, Q., Sheng, Y., Gong, T., 2015. Combined ICESat and CryoSat-2 altimetry for
619 accessing water level dynamics of Tibetan lakes over 2003-2014. *Water (Switzerland)* 7,
620 4685–4700. doi:10.3390/w7094685
- 621 Tauro, F., Petroselli, A., Arcangeletti, E., 2015. Assessment of drone-based surface flow
622 observations. *Hydrol. Process.* 30, 1114–1130. doi:10.1002/hyp.10698
- 623 Tauro, F., Porfiri, M., Grimaldi, S., 2016. Surface flow measurements from drones. *J. Hydrol.*
624 540, 240–245. doi:10.1016/j.jhydrol.2016.06.012
- 625 Villadsen, H., Andersen, O.B., Stenseng, L., Nielsen, K., Knudsen, P., 2015. CryoSat-2 altimetry
626 for river level monitoring — Evaluation in the Ganges–Brahmaputra River basin. *Remote*
627 *Sens. Environ.* 168, 80–89. doi:10.1016/j.rse.2015.05.025
- 628 Watts, A.C., Ambrosia, V.G., Hinkley, E.A., 2012. Unmanned Aircraft Systems in Remote
629 Sensing and Scientific Research: Classification and Considerations of Use. *Remote Sens.*
630 4(6), 1671–1692. doi:10.3390/rs4061671

631 Wingham, D.J., Francis, C.R., Baker, S., Bouzinac, C., Brockley, D., Cullen, R., de Chateau-
632 Thierry, P., Laxon, S.W., Mallow, U., Mavrocordatos, C., Phalippou, L., Ratier, G., Rey, L.,
633 Rostan, F., Viau, P., Wallis, D.W., 2006. CryoSat: A mission to determine the fluctuations
634 in Earth's land and marine ice fields. *Adv. Sp. Res.* 37, 841–871.
635 doi:10.1016/j.asr.2005.07.027

636 Yuen, H., Princen, J., Illingworth, J., Kittler, J., 1990. Comparative study of Hough Transform
637 methods for circle finding. *Image Vis. Comput.* 8, 71–77. doi:10.1016/0262-
638 8856(90)90059-E

639 Zhang, G., Xie, H., 2010. Water level changes of two Tibetan lakes Nam Co and Selin Co from
640 ICESat altimetry data, in: 2010 Second IITA International Conference on Geoscience and
641 Remote Sensing. *IEEE*, pp. 463–466. doi:10.1109/IITA-GRS.2010.5602644

642

643

644 **Appendix A. Calibration of the CLDS**

645 The CLDS needs to be calibrated in order to provide a ranging measurement. Calibration has

646 been performed acquiring multiple range measurements (from 0 to 12 m) using a black vertical

647 wall as calibration target. Since the focal length of the camera is not exactly known, equation (4)

648 must be used and the calibration is used to retrieve the coefficients r_{pp1} and r_0 for converting from

649 pixel units to angular units. The relationships between θ' and the distance from the laser dots to

650 the center of the image (PFC) are shown in Fig. A.1 for each of the laser pointers. Alternatively,

651 Fig. A.2 depicts the relationship between the range to the target and PFC.

Fig. A.1

Fig. A.2

652

653 Fig. A.1 and Fig. A.2 show that the laser pointers' curves are not coincident as a consequence of
654 the slight asymmetry of the layout (imaging sensor of the camera not placed exactly in the
655 middle of the two laser pointers). As confirmed by Fig. A.1, the relationship between PFC and
656 the measured angle is approximately linear for each of the two laser pointers. Calibration has
657 shown an r (Pearson linear correlation coefficient of determination) of 0.99978 and an RMSE
658 (Root Mean Square Error) of 7.16 cm for the blue laser (left laser); an r of 0.99937 and an RMSE
659 of 8.29 cm for the green laser (right laser). Calibration error is displayed in Fig. A.3.

660 Fig. A.3

661

662 Fig. A.4

663

664 Fig. A.3 demonstrates that the advantage of using two laser pointers is improved error
665 assessment. Considering the average of the measurements of the two laser pointers, calibration

666 RMSE is reduced to 5.61 cm. When range to water surface has to be retrieved, the precise
667 computation of PFC is more problematic than during the simple calibration procedure. Indeed,
668 while laser dots can be normally identified as in Fig. A.4 (a), laser dots on the water surface
669 might have contours that are less defined as in Fig. A.4 (b). Sometimes even multiple laser dots
670 are visible, as shown in Fig. A.4 (c). This is caused by: i) atmospheric scattering processes, ii)
671 scattering processes due to water waviness iii) vibrations of the UAV. The laser light reflected
672 from the bottom is occasionally visible in the image, especially in case of shallow or very clear
673 water, as shown in Fig. A.4 (d). Experiments showed that the uncertainty in the PFC increases
674 with the range to water surface. This is displayed in Fig. A.5 with the curve $PFC-\sigma_{PFC}$. Fig. A.5
675 clearly shows that the green laser exhibits larger uncertainty than the blue laser since green
676 wavelengths are scattered to a greater extent than blue wavelengths. The expected uncertainty in
677 the range can be estimated using the derivative of the range function as shown in equation (A.1).

$$\sigma(range) = \frac{\partial range}{\partial (PFC)} \sigma(PFC) \quad (A.1)$$

Fig. A.5

Fig. A.6

678 Fig. A.6 shows that the uncertainty of the range estimate increases with the range to water
679 surface. This is a consequence of: i) the derivative of the curve in Fig. A.2 that increases in
680 absolute value for longer ranges (small inaccuracy in PFC determines high imprecision in the
681 range observation). The derivative is lower in absolute terms for the blue laser, because of the
682 prototype layout. ii) Increasing uncertainty of the PFC with increasing range (i.e. decreasing
683 PFC).

684

685

686 *Appendix B. Experimental settings*

687

688

689 In Table B.1 we report the location, the date and time of the day, the environmental conditions
690 and the water flow speed for each of the static tests. The mean value and the standard deviation
691 of the measurements are shown in Figure 8.

692 Here Table B.1

693 Illumination conditions are reported in the table because they affect visibility of the laser dots on
694 the water surface. This factor has been critical only in case of sun glint conditions during which
695 laser dots are hardly identifiable. On the other hand, wind stress and current can affect water
696 surface roughness and change the intensity of the backscattered radar signal.

697 Estimates of beam divergence for the different sensors were obtained from tests above a
698 cylindrical water well of diameter (D) equal to 0.7 m. The sensors were placed exactly in the
699 middle of the water well as shown in Fig. B.1. The initial range between the sensors and the
700 water surface was 0.5 m. Subsequently, the well was pumped to gradually increase the range to
701 the water surface. Beam divergence (φ) was then computed according to equation B.1.

$$\varphi = 2 * \tan^{-1} \frac{D}{2 \cdot r_c} \quad (B.1)$$

702 In equation B.1, r_c is the critical range i.e. the range at which the sensor first produced erroneous
703 results because of interference with the well walls. Fig. B.1 provides an illustration of the
704 experimental setup.

705

706 Fig. B.1

707

708 While the CLDS was able to retrieve the range to water surface for all water levels (beam width
709 is constant and equal to the arm length), the beam divergences of the radar and the sonar were
710 estimated using this method. For the radar, interferences started to occur at a range of 1.3 m, and
711 for the sonar at 1 m. Equation B.1, then gives beam divergence of the radar as ca. 30° and beam
712 divergence for the sonar as ca. 40° .

713 Table B.2 shows the flight records for the tests conducted over the lake to estimate the airborne
714 accuracy of the system.

715

716 Table B.2

717

718

719 As Table B.2 shows, the GNSS satellite cut-off angle settings are different between the flights.
720 The cut-off angle showed an influence on the position accuracy, and thus on the water level
721 measurements, up to 1-2 cm. Larger cut-off angles reduce the number of satellites in the field of
722 view of the GNSS antenna, while smaller cut-off angles might increase multi-path effects (e.g.
723 GNSS signal reflected by the water surface).

724 Average and vertical speed was varied between the different flights to test the synchronization
725 between the GNSS system and the different sensors. Indeed, since water level is constant in the
726 lake, when the drone rapidly changes its altitude, equivalent variations should be recorded by the
727 ranging sensors and the GNSS system. Synchronization between the radar, sonar and the GNSS
728 was obtained at the 30 ms level, while synchronization with the CLDS was obtained at the 0.2 s

729 level. The synchronization between the GNSS system and the CLDS is slightly worse because,
730 even though the SBC registers the time at which the camera is triggered, the actual time that the
731 CMOS camera needs to take a picture is unknown.

732

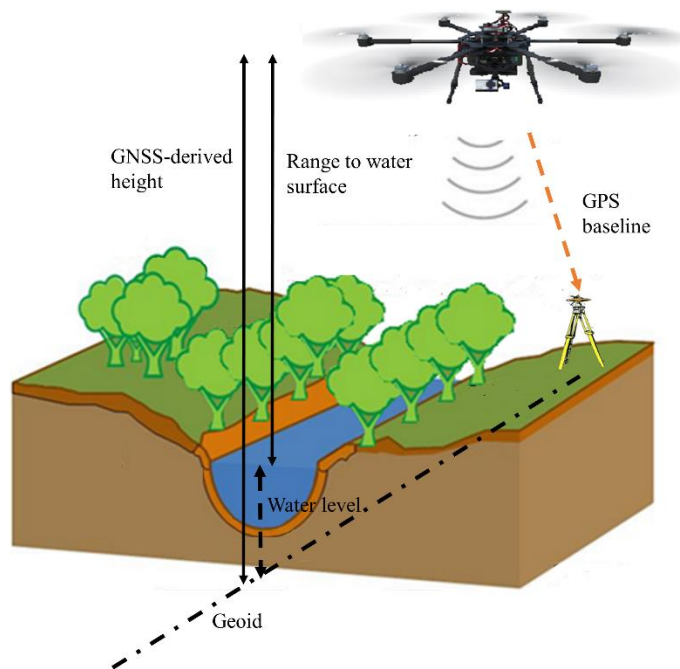
733

734

735

Figures

736

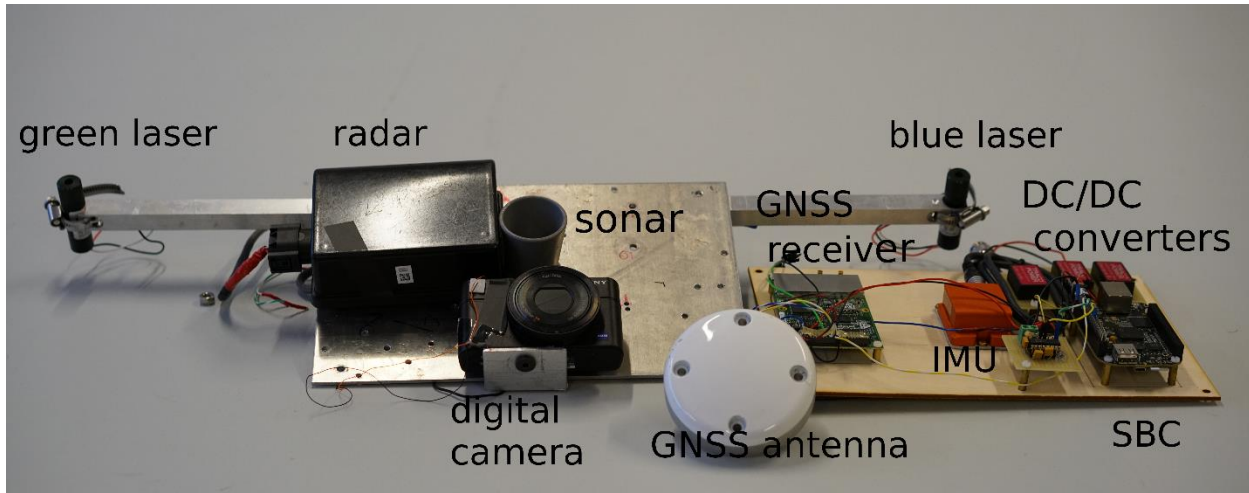


737

738

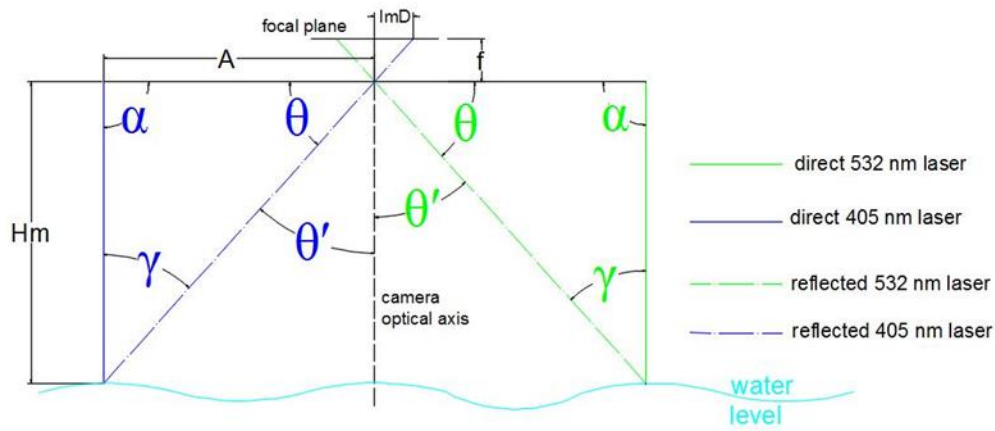
739 Fig. 1. Illustration of measurement principle for retrieving water level. The system includes: i) the UAV, ii) the
740 sensors to measure the range from the UAV to the water surface, iii) a GNSS receiver on board the UAV providing
741 accurate vertical and horizontal position. Centimeter-level position accuracy is obtained through the installation of
742 an in-situ GNSS master station providing corrections for a kinematic post-processed solution.

743



744

745 Fig. 2. Picture of the drone payload. It includes the three tested sensors (CLDS, radar and sonar), the GNSS system
746 (antenna and receiver), the IMU, the Single Board Computer (SBC) and the power conversion units (DC/DC
747 converters).



748

749

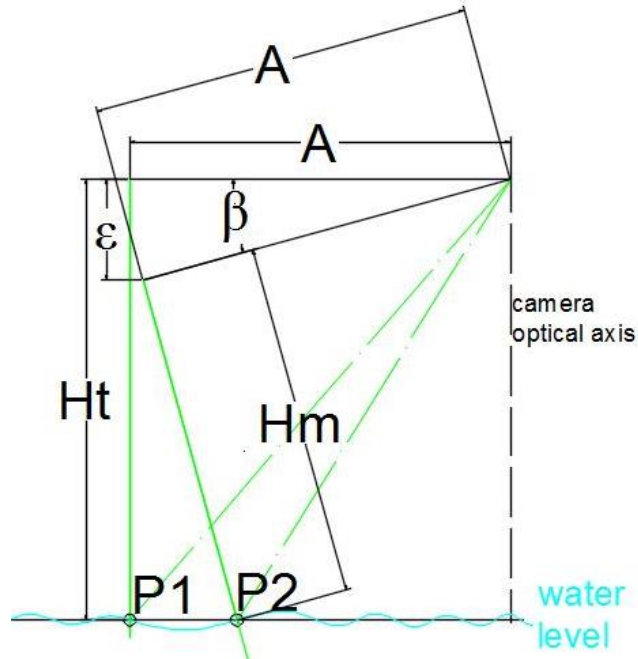
750

751

752

753 Fig. 3. Geometric configuration of the CLDS solution. A is the distance between the center of the camera and each
754 of the laser pointers. α is the angle between each of the lasers and the focal plane of the camera. H_m is the distance
755 between the camera and the water surface. ImD is the distance between the center of the image focal plane and each
756 of the recorded laser light dots. f is the focal length of the camera. θ' is the reflection angle. θ is its angle between the
757 axis of the CLDS and the reflected ray. γ is the angle between incident and reflected ray. If α is 90° (as in the
758 figure), γ is equal to θ' .

759



760

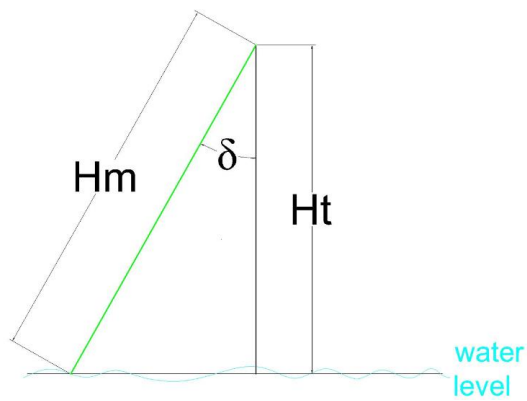
761

762 Fig. 4. Tilting angle: β is the angle between the horizontal line and the plane where the lasers and the camera are
 763 located.

764

765

766

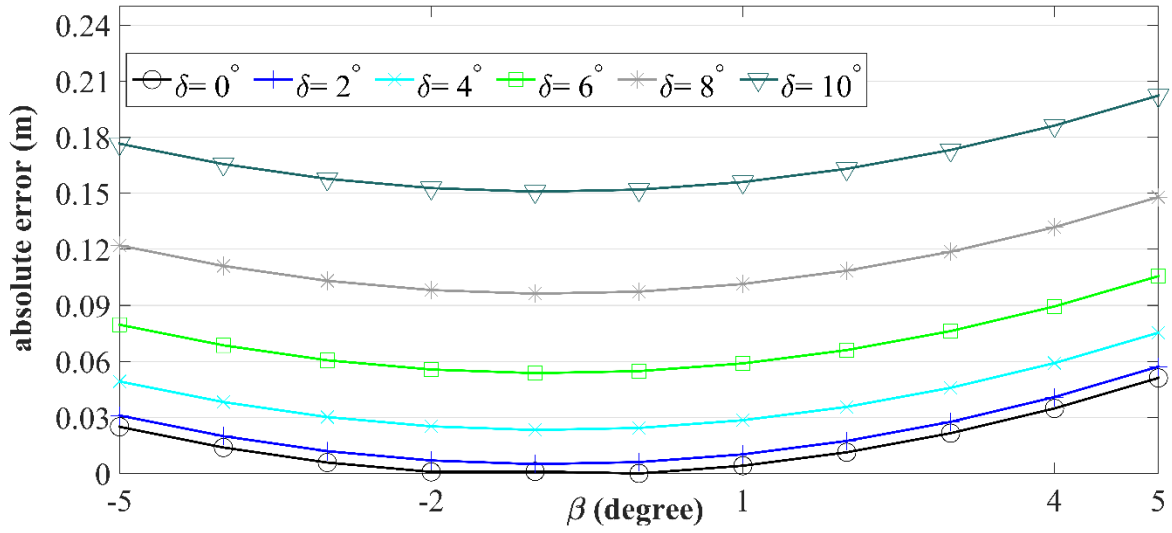


767

768

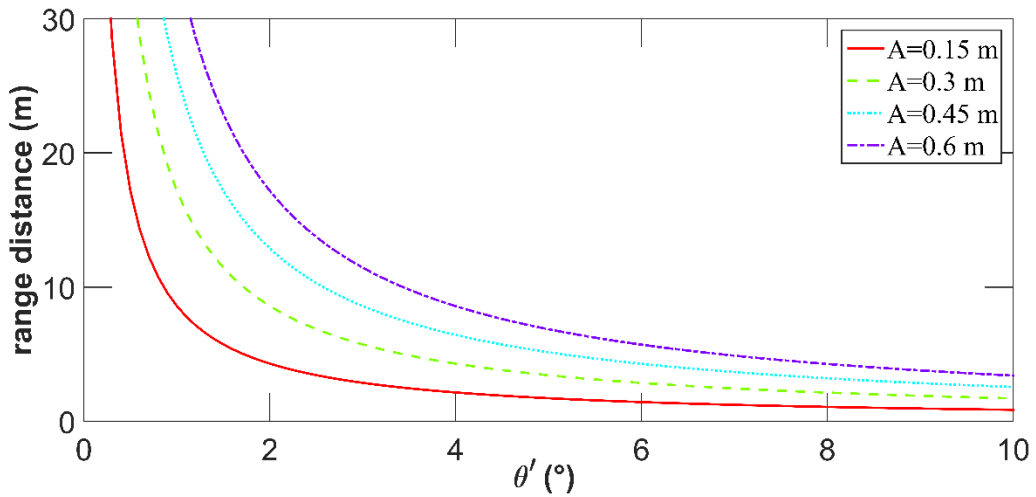
769 Fig. 5. Rotation angle: δ is the angle between the vertical line and optical axis of the camera.

770



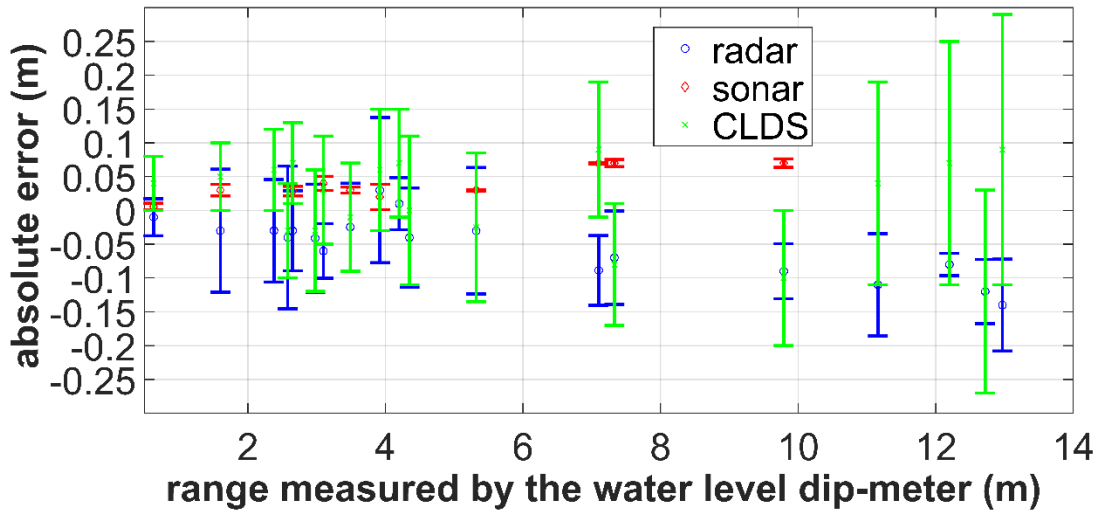
771
772
773
774
775
776
777
778

Fig. 6. Error as a function of displacement angles. Absolute error is shown for different tilting (β) and rotation (δ) angles at 10 m range.



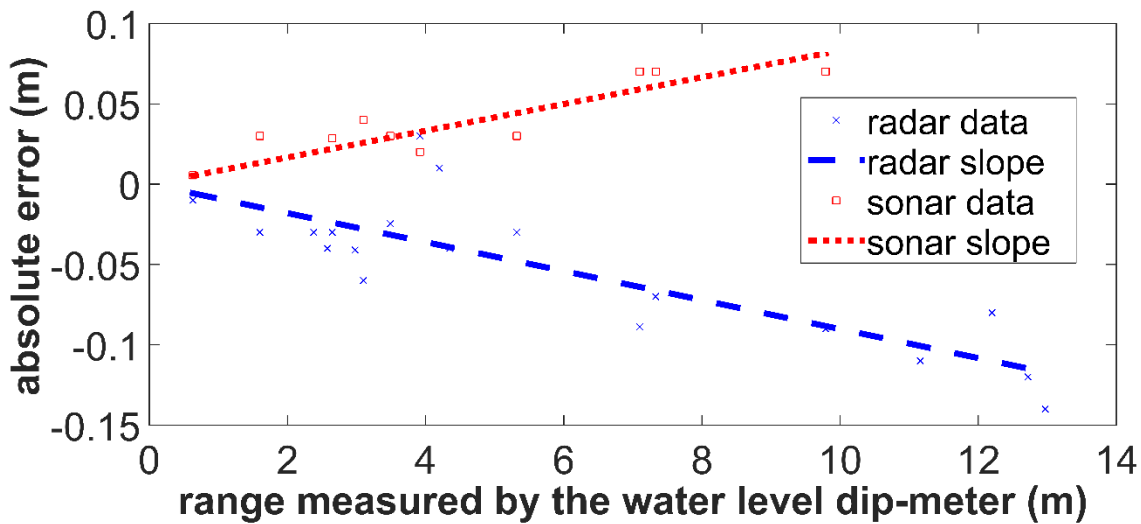
779
780
781
782
783
784

Fig. 7. Range distance as a function of the θ' angle. The range function depends on the different length values of A, which is the distance between the laser source and the camera.



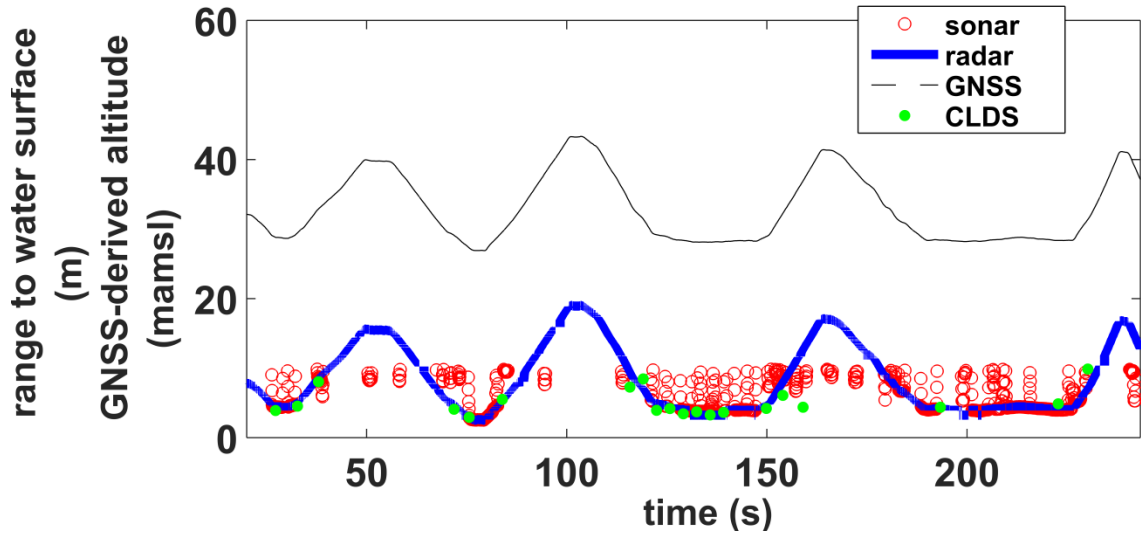
785
786
787
788
789
790

Fig. 8. Absolute error as a function of the range measured by each of the ranging sensors. Absolute error is computed using the water level dip meter as reference. The marker is the average error (bias) of all measurements taken for a specific range, while the bar shows the standard deviation.



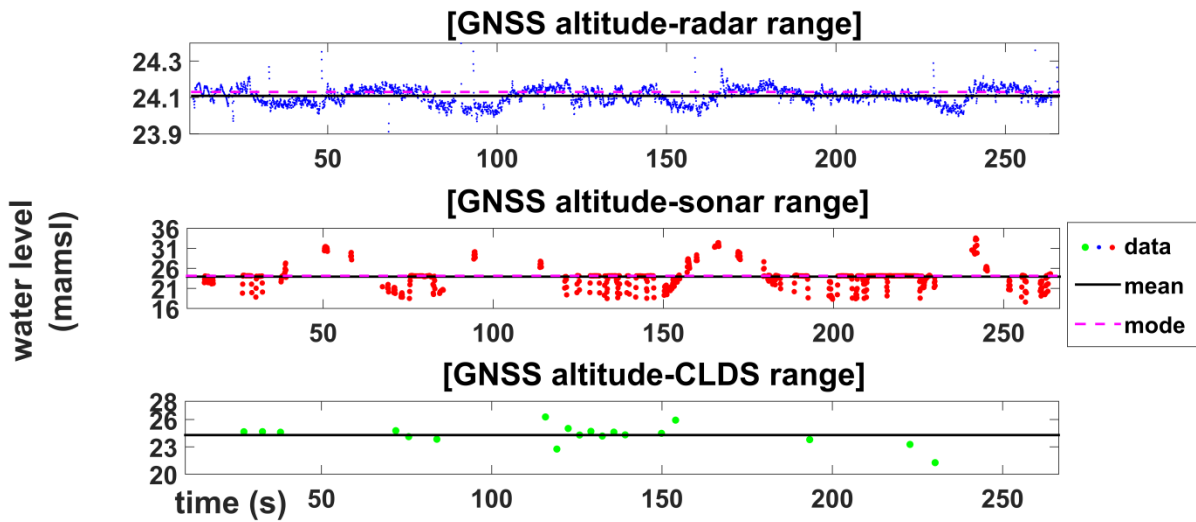
791
792
793
794
795
796
797
798

Fig. 9. Sonar and radar errors as a function of the range. Dots represent the measurements acquired by the radar and the sonar. The regression line shows that the absolute error is a function of the range.



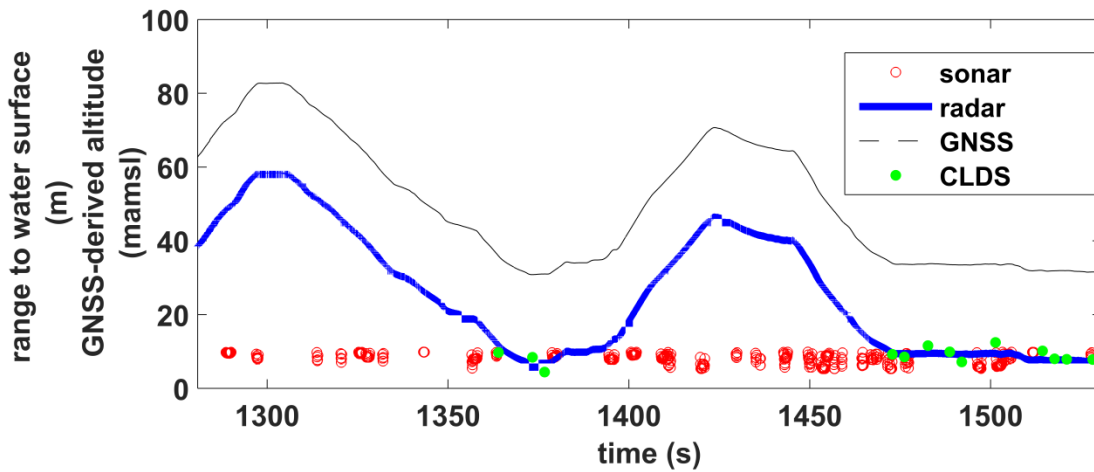
799
800
801
802
803
804

Fig. 10. Observations retrieved during the flight on April 4, 2016. The plot shows the range measured by the radar (blue), sonar (red), CLDS (green) in meter (m) to the water surface, and the drone altitude retrieved by the GNSS (black) in meter above mean sea level (mamsl).



805
806
807
808
809
810
811

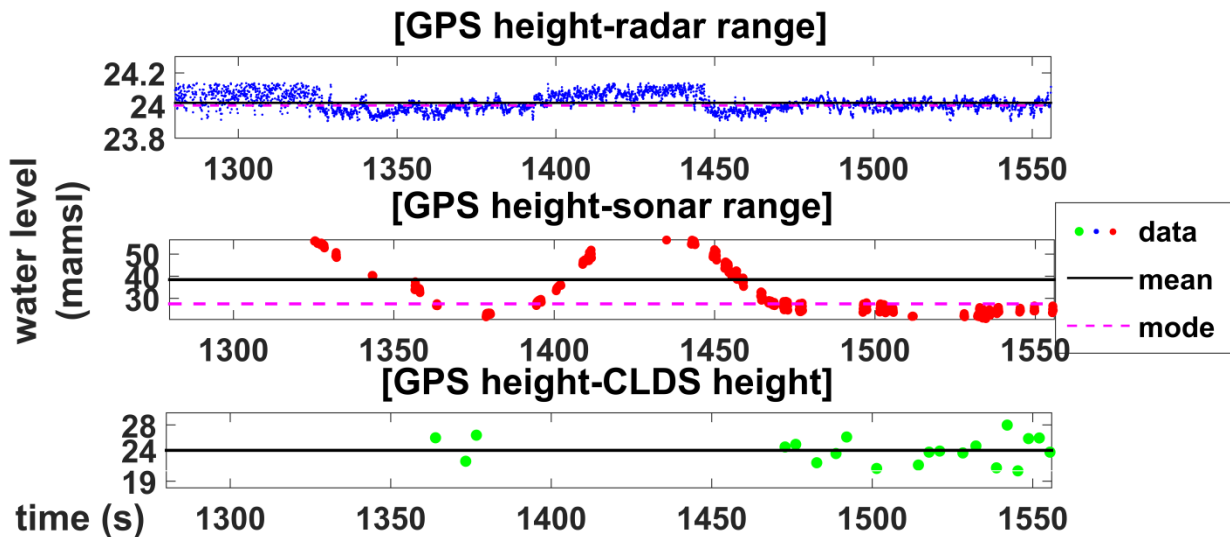
Fig. 11. Water level (mamsl) observations retrieved during the flight on April 4, 2016. Each of plots shows the water level observations measured by subtracting the range retrieved by each of the sensors (radar, sonar, CLDS) from the GNSS altitude. In each plot, the black line is the mean of the water level observations and the magenta line is the mode of those observations.



812

813 Fig. 12. Observations retrieved during the flight on May 27, 2016. The plot shows the range measured by the radar
 814 (blue), sonar (red), CLDS (green) in meter (m) to the water surface, and the drone altitude retrieved by the GNSS
 815 (black) in meter above mean sea level (mamsl).

816



817

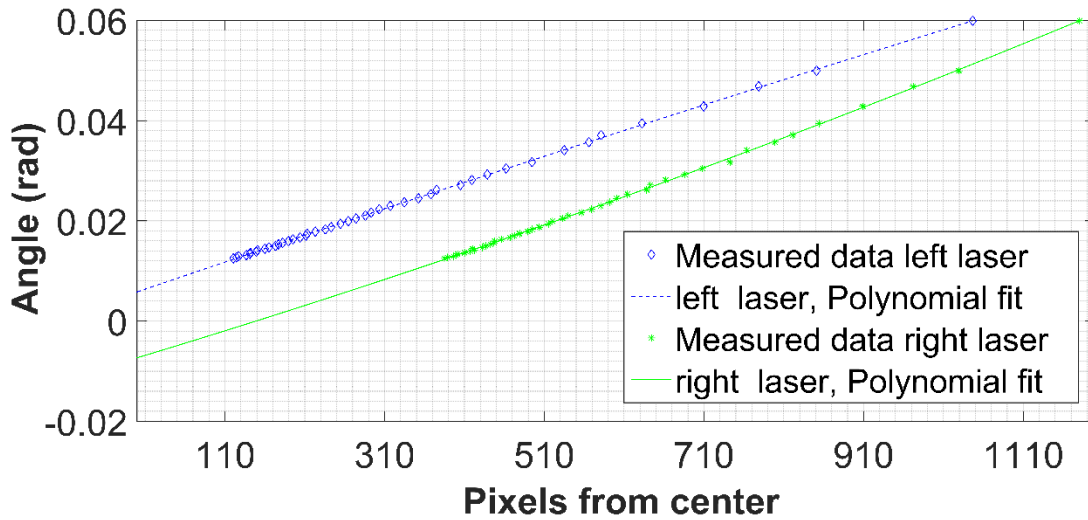
818

819 Fig. 13. Water level (mamsl) observations retrieved during the flight on May 27, 2016. Each of plots shows the
 820 water level observations measured by subtracting the range retrieved by each of the sensors (radar, sonar, CLDS)
 821 from the GNSS-derived altitude. In each plot, the black line is the mean of the water level observations and the
 822 magenta line is the mode of those observations.

823

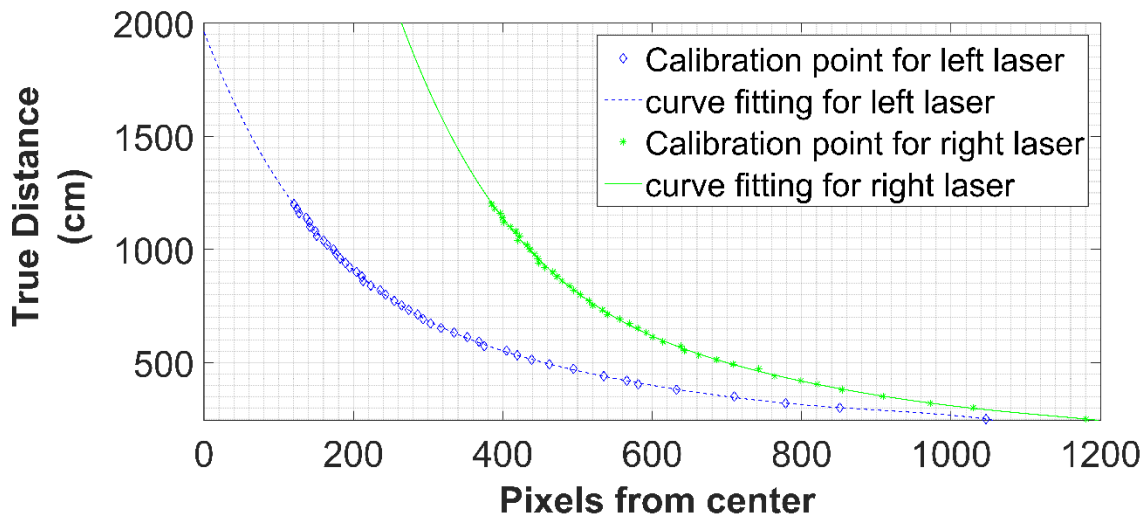
824

825



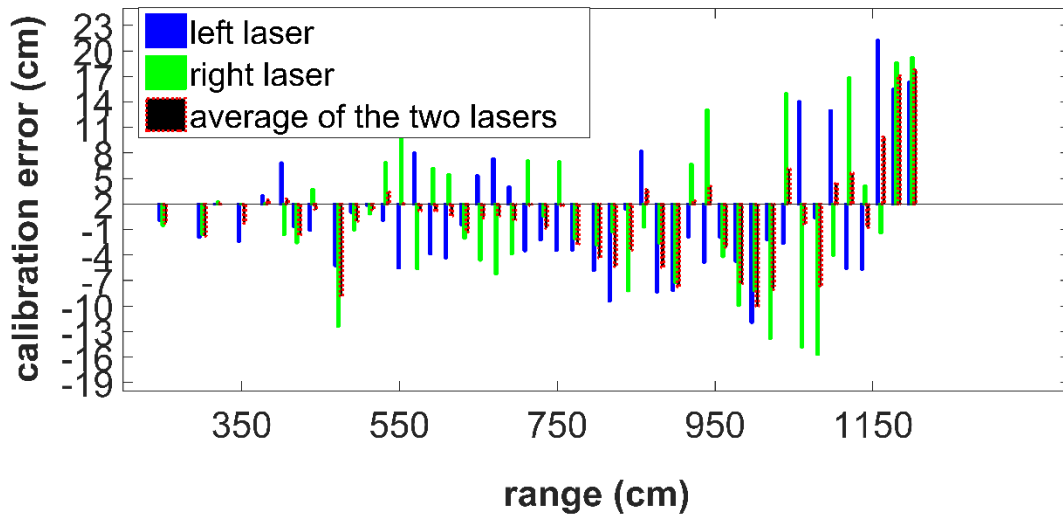
826
827
828
829

Fig. A.1. Relationship between the measuring angle θ' and PFC.



830
831
832
833
834
835
836
837

Fig. A.2. Relationship between the range to the target and PFC.



838

839

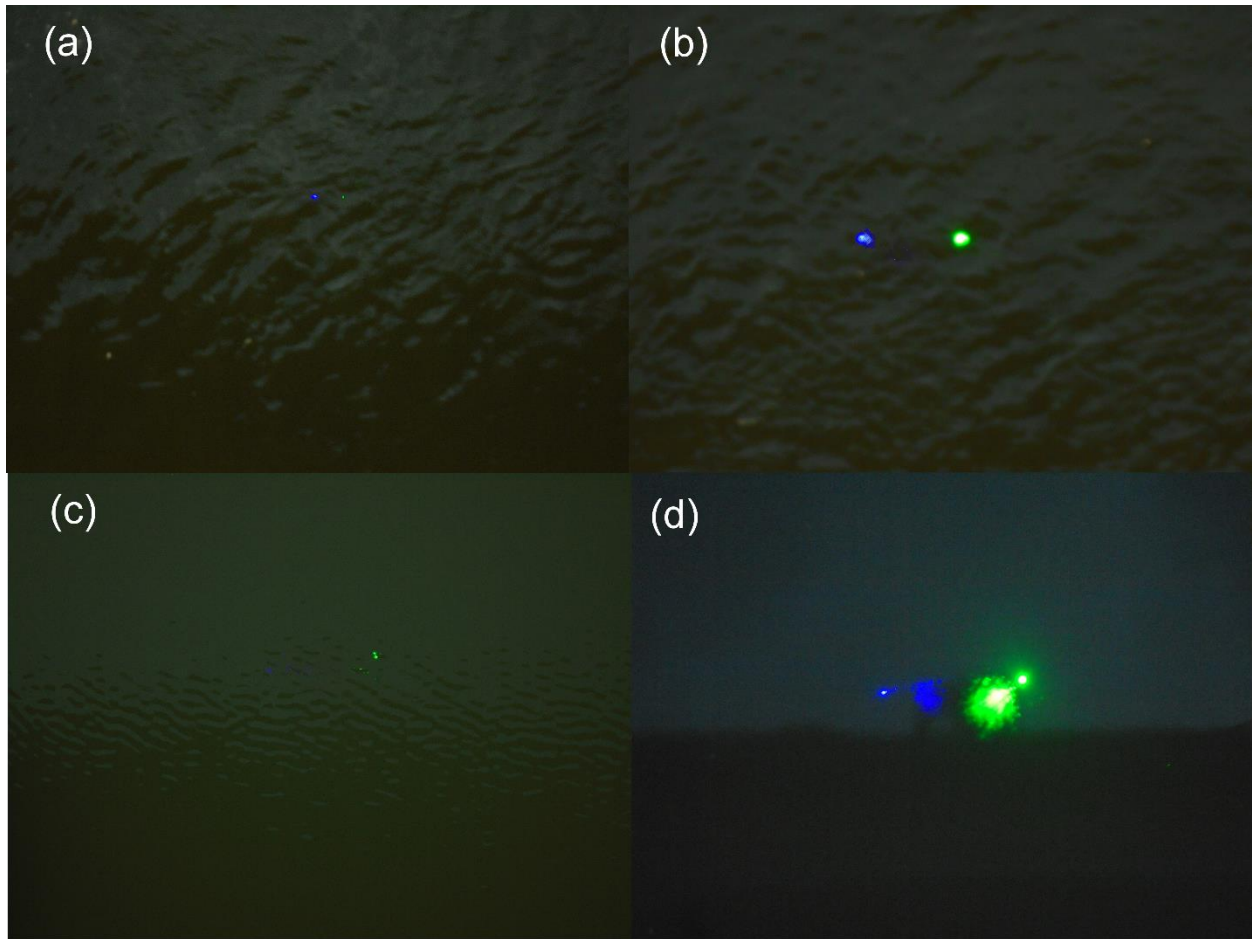
840

Fig. A.3. Calibration error for left laser (blue column), right laser (green column) and for the average (red column) between the two laser pointers.

841

842

843



844

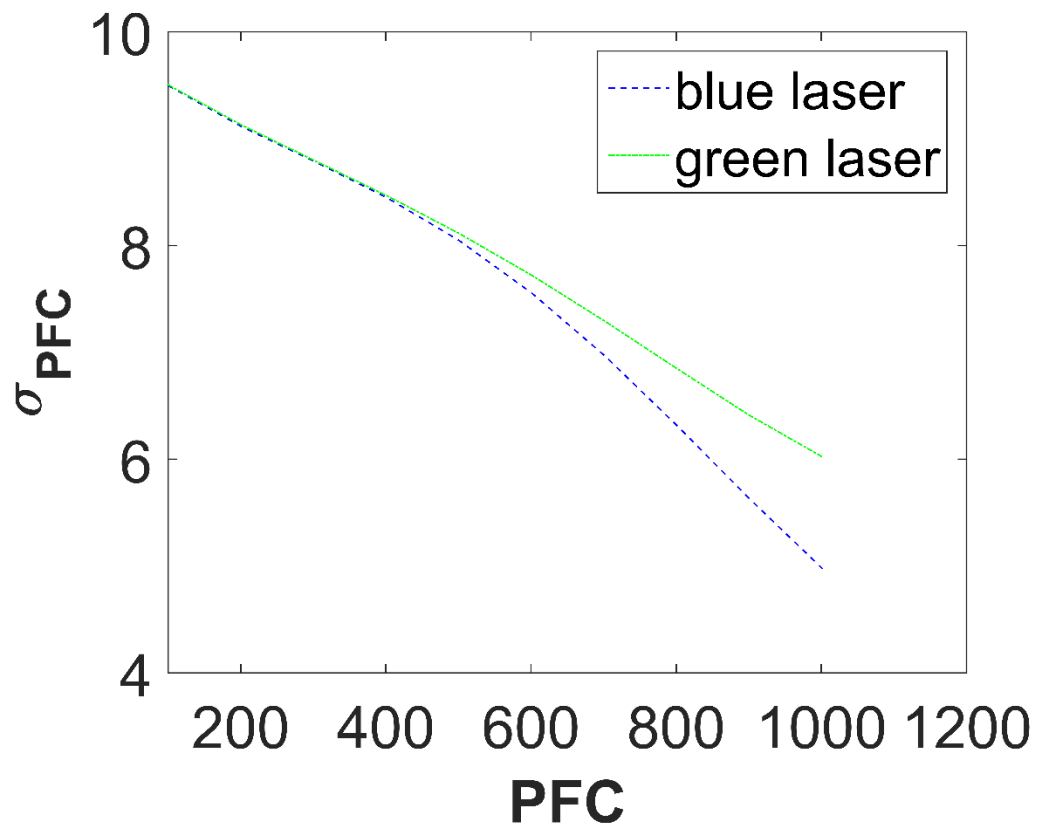
845

846

847

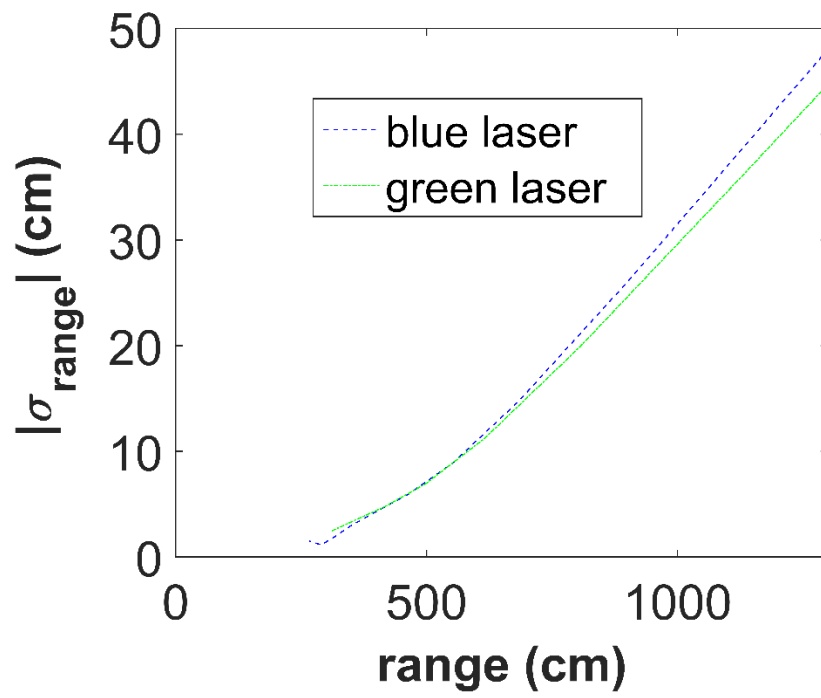
848

Fig. A.4. Airborne image of water surface taken by the CLDS. (a) the two laser dots are clearly identifiable (b) larger laser dots with contours that are less identifiable (c) multiple green laser dots caused by multiple reflection and scattering processes (d) laser light is reflected by the bottom (larger dots) and by the surface (smaller dots)



849
850
851
852

Fig. A.5. Uncertainty (σ_{PFC}) in computing the number of pixels as a function of PFC, for green and blue laser.



853

854

855

856 Fig. A.6. Absolute uncertainty in range measurement ($|\sigma_{\text{range}}|$) as a function of the range to the target, for green
857 and blue laser.

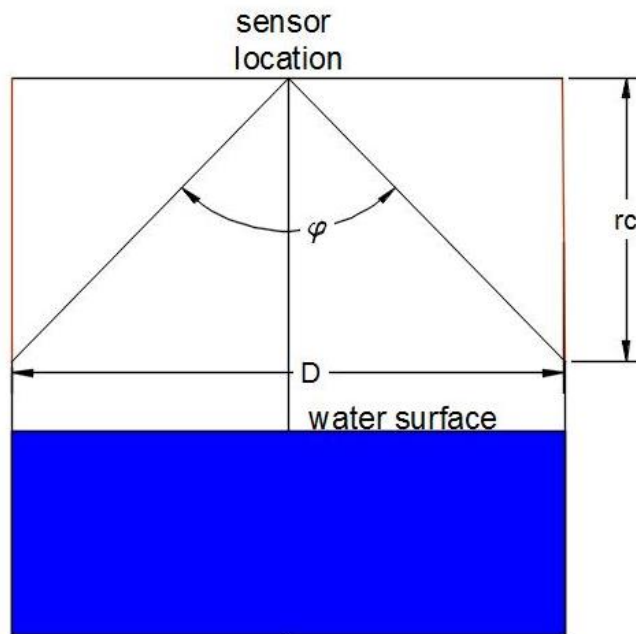
858

859

860

861

862



863

864

865 Fig. B.1. Schematic representation of the test conducted over the water well to retrieve beam divergence (φ) for each
 866 of the sensors. D is the diameter of the water well, r_c is the critical range.

867

868 Tables

869

870

871 *Table 1. Technical performance of the sensors and of the GNSS receiver when tested in static mode.*

	mean absolute error (percentage of the range)	standard deviation of the stack	Maximum ranging distance	Beam divergence
Radar	-1.09%	0.064 m	60 m near field 200 m far field	$\sim 30^\circ$
Sonar	0.98%	0.007 m	10 m	$> 40^\circ$
CLDS	1.5%	2.3 % of the range	13 m	negligible
GNSS receiver	negligible	Vertical	-----	-----

coordinates : 4-6

cm at 2 sigma

872

873

874

875 *Table 2. Summary of the test flights over the lake. Each flight is named with the date (corresponding year is 2016). Ground truth*

876 *was measured with a RTK GNSS rover station connected to the network of reference stations. Statistics concern the water level*

877 *observations measured by subtracting the GNSS flight altitude from the range to water surface measured by each of the sensors.*

878 *Statistics are computed after removal of the observations that lie beyond 2σ .*

		Flight date (dd/mm/2016)				
Flight statistics		17/03	04/04	13/04	05/13	27/05
Ground truth (mamsl)		missing	24.10±0.0 6	24.13±0.0 6	24.04±0.0 6	24.01±0.0 6
Mean value (mamsl) of water level retrieved by	radar	24.10	24.11	24.20	24.11	24.02
	sonar	23.50	23.93	20.01	27.05	38.45
	CLDS	missing	24.29	24.81	24.82	23.93
Mode value (mamsl) of water level retrieved by	radar	24.18	24.13	24.10	24.12	24.00
	sonar	24.40	24.14	24.08	24.65	27.50
	CLDS	missing	21.27	24.56	24.41	20.66
Standard Deviation (m) in water level retrieved by	radar	0.07	0.05	0.08	0.09	0.05
	sonar	0.80	2.31	1.3	0.36	14.42
	CLDS	missing	1.08	0.95	1.68	2.05

879

880

881

882

883

884

885

886

887

888
889
890
891

Table 3. Accuracy and ground footprint of different techniques for observing water level

Location	Technique	Footprint	Accuracy	Reference
Airborne	LIDARs	20 cm-1 m	4-22 cm	(Hopkinson et al., 2011)
Spaceborne	laser altimetry (e.g. ICESat)	50–90 m	10 cm	(Phan et al., 2012)
Spaceborne	radar altimetry (e.g. ERS2, Envisat, Topex/Poseidon)	400 m-2 km	30-60 cm	(Frappart et al., 2006)
Ground-based	radar/sonar/pressure transducers	negligible	1 mm-10 cm	Widely known metrology
UAV-borne	radar altimetry	negligible	5-7 cm	Methodology described in this paper

892

893 Table B.1. Locations, settings and environmental conditions during static (on ground) tests. Coordinates are in WGS84. Country
894 is either Denmark (DK) or Italy (IT). Range (m) is the value measured by the water level dip meter. Water speed has qualitatively
895 been classified into no speed (still water), low (less than 0.4 m/s), medium (between 0.4 and 1 m/s), and high speed (more than 1
896 m/s). Wind speed has been qualitatively classified into no wind, low (wind less than 2 m/s), medium (between 2 m/s and 8 m/s),
897 and high wind speed (more than 8 m/s). Illumination has been qualitatively classified into artificial lightening, low (less than 20
898 000 lux), medium (between 20 000 and 50 000 lux), and high illumination (more than 50 000 lux)

Latitude	Longitude	River	Country	Range to water	Date (dd/mm/2015)	Time of the day (hh:mm)	Flow speed	Wind	Illumination
55.783431	12.515610	Laboratory	DK	0.63	2/11	11:20	no	no	artificial
55.775211	12.470266	Mølleåen	DK	1.60	20/11	13:30	low	medium	low
55.775211	12.470266	Mølleåen	DK	2.38	20/11	11:41	low	medium	low
55.775211	12.470266	Mølleåen	DK	2.58	20/11	11:52	low	medium	low
55.775211	12.470266	Mølleåen	DK	2.65	10/10	11:20	low	high	low
55.775211	12.470266	Mølleåen	DK	2.98	1/10	14:10	low	medium	low
55.775211	12.470266	Mølleåen	DK	3.10	10/10	11:25	low	high	low
55.775211	12.470266	Mølleåen	DK	3.49	10/10	11:49	low	high	low
44.909645	10.991254	Sabbioncello	IT	3.92	22/12	16:00	low	low	low
55.775211	12.470266	Mølleåen	DK	4.20	10/10	14:10	low	high	medium
55.775211	12.470266	Mølleåen	DK	4.35	1/10	14:33	low	medium	low
45.038994	10.965141	Canale Bonifica	IT	5.32	22/12	13:00	low	low	medium

		Parmigiana,								
45.029723	10.959166	Canale della Bonifica Reggiana Montovana	IT	7.10	22/12	14:05	low	low	low	
45.029726	10.960432	Canale della Bonifica Parmigiana	IT	7.33	22/12	9:30	low	low	low	
44.650573	10.794755	Secchia	IT	9.79	29/10	12:00	medium	medium	medium	
44.821261	10.994579	Secchia	IT	11.16	29/10	12:50	medium	medium	high	
44.67578	10.860146	Secchia	IT	12.20	29/10	13:50	medium	medium	medium	
45.008365	10.977453	Secchia	IT	12.72	29/10	20:30	medium	medium	low	
44.727259	11.045292	Panaro	IT	12.97	29/10	8:30	medium	low	low	

899

900 Table B.2. Summary of the test flights over the lake.

Flight statistics	Flight date (dd/mm/2016)				
	17/03	04/04	13/04	05/13	27/05
Take-off time (hh:mm)	15:00	12:20	13:20	13:00	12:00
Flight time over water (s)	500	270	200	250	260
Minimum-Maximum flight height (meter above water surface)	3-28	4-18.5	5-60	8-48	9-58
Average horizontal speed (m/s)	2	3	4	1	2
Average vertical speed (m/s)	0.1	1.1	1	0.3	0.3
Maximum vertical speed (m/s)	1	2	3	1.5	1
GPS cut-off angle (degree)	10	13	14	15	15

901

902

903